Volume 19
Number 2
27 January 2026
Pages 401–732

Energy & Environmental Science

rsc.li/ees

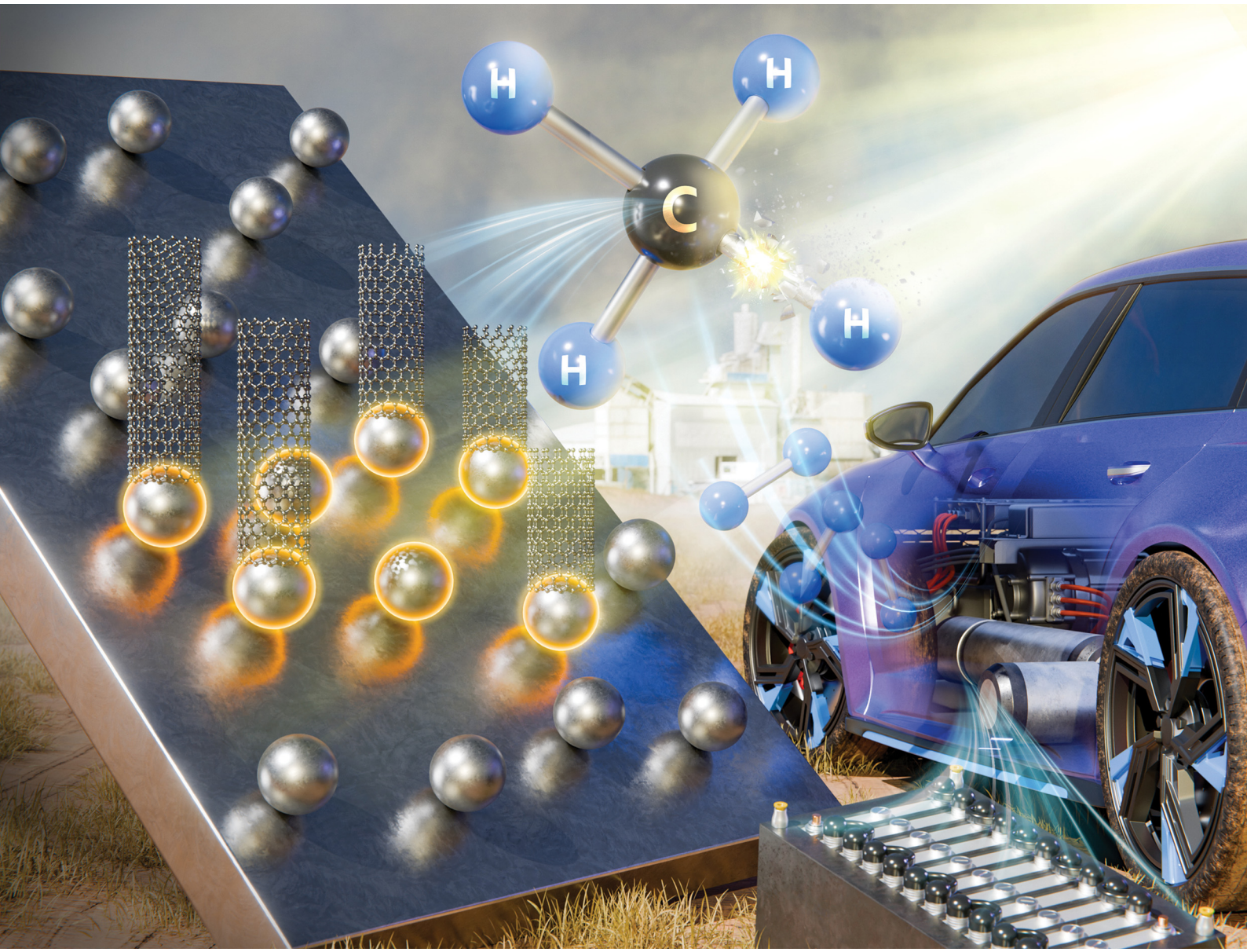

ISSN 1754-5706

ROYAL SOCIETY OF CHEMISTRY

PAPER
Abdelaziz Gouda, Mohini Sain, Geoffrey Ozin *et al.*
Methane photolysis to clean hydrogen and carbon nanotubes

Energy & Environmental Science

ROYAL SOCIETY OF CHEMISTRY

PAPER

View Article Online
View Journal | View Issue

Cite this: *Energy Environ. Sci.*, 2026, **19**, 496

Methane photolysis to clean hydrogen and carbon nanotubes

Abdelaziz Gouda,*[abc] Juan Manuel Restrepo-Flórez,[d] Abhinav Mohan,[abc] Otavio Augusto Titton Dias,[c] Andrew Wang,[a] Camilo J. Viasus Perez,[ae] Jessica Ye,[ac] Tamlyn Slocombe,[a] Vijay K. Tomer,[c] Jiabao Shen,[f] Nhat Truong Nguyen,[g] Nazir Kherani,[f] Mohamad Hmadeh,[ah] Alán Aspuru-Guzik,[abi] Mohini Sain*[bc] and Geoffrey Ozin*[ab]

Received 16th April 2025,
Accepted 10th November 2025

DOI: 10.1039/d5ee02120k

rsc.li/ees

The transition to sustainable hydrogen production is critical to decarbonizing the global energy system and reducing reliance on carbon-intensive methods such as steam methane reforming (SMR). Methane pyrolysis has emerged as a lower-emission alternative, yet its viability is constrained by the extreme temperatures required (600–1200 °C) and associated energy demands. Here, we present methane photolysis, $CH_4(g) + h\nu \rightarrow C(s) + 2H_2(g)$, as a novel, light-driven pathway for simultaneous hydrogen and carbon nanotube production. Operating at ambient conditions and powered by LED illumination, this scalable and continuous process selectively yields clean hydrogen with a maximum hydrogen production rate of 17.74 ± 1.71 mol cm^{-2} h^{-1} and high-value carbon nanotubes (CNTs) achieving yields of approximately 8.0 g CNT per g catalyst at a production rate of $\sim 0.150 \pm 0.001$ g h^{-1}, while circumventing the thermal and carbon burdens of conventional methods. Compared to water electrolysis, our approach requires approximately 70% less energy per kilogram of H_2 produced. For CNTs, the energy savings reach ~74% relative to conventional methods such as fluidized-bed chemical vapor deposition. Techno-economic and life-cycle assessments demonstrate its potential as a scalable, energy-efficient alternative for decentralized hydrogen and carbon nanomaterial synthesis, with implications for cleaner fuel production and circular carbon utilization.

Broader context

The global shift toward sustainable hydrogen production is essential for decarbonizing energy systems and achieving climate goals. While current industrial methods like steam methane reforming and high-temperature pyrolysis can produce hydrogen at scale, they are energy-intensive and carbon-emitting. This study introduces a light-driven methane photolysis process that operates at ambient conditions to simultaneously generate clean hydrogen and valuable multi-walled carbon nanotubes (MWCNTs). Unlike conventional approaches, this method eliminates the need for high temperatures, reducing energy input by up to 70% for hydrogen and 74% for CNTs. Techno-economic and life cycle analyses show that the light-driven process not only lowers the environmental footprint but also enhances economic feasibility, particularly under solar or LED operation. Beyond hydrogen, the co-produced MWCNTs offer sustainable value as next-generation materials in batteries and electrical systems, potentially displacing copper. By integrating system energy requirements, carbon valorization, and economic viability, this approach represents a transformative advancement in clean hydrogen and carbon nanomaterial production.

[a] *Department of Chemistry, University of Toronto, 80 Saint George St., Toronto, Ontario M5S 3H6, Canada. E-mail: Abdelaziz.gouda@utoronto.ca, g.ozin@utoronto.ca*
[b] *Department of Applied Chemistry and Chemical Engineering, University of Toronto, 200 College St., Toronto, ON M5S 3E5, Canada. E-mail: m.Sain@utoronto.ca*
[c] *Department of Mechanical and Industrial Engineering, University of Toronto, 5 King's College Rd, Toronto, ON, M5S 3G8, Canada*
[d] *Department of Chemical Engineering, University of Florida, Gainesville, Florida 32611, USA*
[e] *Grupo de Investigación en Química de Coordinación y Bioinorgánica, Departamento de Química, Facultad de Ciencias, Universidad Nacional de Colombia, Av. Carrera 30 # 45-03, Sede Bogotá, Colombia*
[f] *Department of Electrical and Computing Engineering, University of Toronto, 10 King's College Road, Toronto, Ontario M5S 3G4, Canada*
[g] *Department of Chemical and Material Engineering, Gina Cody School of Engineering and Computer Science, Concordia University, Montreal, Quebec, Canada*
[h] *Department of Chemistry, Faculty of Arts and Sciences, American University of Beirut, P.O. Box 11-0236, Beirut 1107 2020, Lebanon*
[i] *Department of Computer Science, University of Toronto, Sandford Fleming Building, 10 King's College Road, Toronto, Ontario M5S 3G4, Canada*

Introduction

The global shift towards renewable energy sources is underscoring the urgent need for sustainable methods of hydrogen production, as hydrogen is increasingly regarded as a critical energy carrier in the transition to a low-carbon future.[1,2] As a versatile fuel, hydrogen has the potential to decarbonize a wide array of industries, from transportation to heavy manufacturing, all while facilitating the storage and transport of renewable energy.[3] However, the predominant industrial methods for hydrogen production, particularly steam methane reforming (SMR), face significant challenges.[4,5] SMR relies on fossil fuels and is associated with high energy consumption and substantial CO_2 emissions, undermining its role in achieving global sustainability goals.

Steam-methane reforming

$$\begin{aligned} &CH_{4(g)} + 2H_2O_{(g)} \rightarrow CO_{2(g)} + 4H_{2(g)} \\ &\Delta H^0_{25^\circ C} = 252.75 \text{ kJ mol}^{-1} \text{ of } CH_4 \end{aligned} \quad (1)$$

One such promising alternative is methane pyrolysis, which can produce hydrogen without generating CO_2 by decomposing methane (CH_4) into hydrogen (H_2) and solid carbon.[6–8]

Methane pyrolysis

$$\begin{aligned} &CH_{4(g)} \rightarrow C_{(s)} + 2H_{2(g)} \\ &\Delta H^0_{25^\circ C} = 74.90 \text{ kJ mol}^{-1} \text{ of } CH_4 \end{aligned} \quad (2)$$

Unlike SMR, methane pyrolysis avoids direct CO_2 emissions by utilizing high temperatures (600–1200 °C) to induce the necessary chemical reactions. While this process offers a cleaner alternative to SMR, the intensive thermal requirements result in substantial energy inputs, limiting its economic viability and scalability, especially when considering the broader goal of decarbonizing the energy sector. Consequently, there is an increasing demand for methods that can overcome the energy-intensive nature of traditional pyrolysis while still enabling efficient, low-carbon hydrogen production.

Another promising thermochemical approach employs concentrated solar to crack methane around 1600 K in a particle flow reactor using light intensities equivalent to 1720 suns to produce hydrogen (H_2) and carbon filaments.[9] Solar thermal cracking of methane of this kind has been explored in different reactor configurations, such as rotary beds and roll-to-roll reactors.[10–12]

Methane photolysis, described herein by contrast, is a photocatalytic (photochemical/photothermal) process in which light under ambient conditions is used to dissociate methane into hydrogen and carbon nanotubes. The direct use of photons eliminates the need for high temperatures, significantly reducing the energy input required compared to the aforementioned methods. The carbon nanotube coproduct brings dual value to the process with applications in energy storage, electronics, and advanced materials science.[13–15] The process can be scaled and operated continuously with light-emitting diodes, thereby circumventing solar intermittency. It outperforms methane steam reforming and water electrolysis in energy requirements, environmental impact, and cost-effectiveness, as validated by system energy requirements calculations, techno-economic and life-cycle analyses (TEA–LCA). A comparative summary of similar work in the literature, including methane pyrolysis and concentrated solar-driven cracking approaches, is presented in Table S1. To the best of our knowledge, this is the first report of methane photolysis driven by low-intensity light irradiation that enables the simultaneous production of high-value CNTs and clean hydrogen, with CNTs mechanically separable from the catalyst, eliminating the need for chemical post-processing.

Results and discussions

Methane photolysis performance evaluation

Activity was initially evaluated using a 300 W Xe lamp (up to 30 W cm^2 irradiation intensity, where 0.1 W cm^2 is equal to 1 sun; Xe lamp spectra in Fig. 1a) in a fixed-bed reactor (Fig. S1 and S2). Methane photolysis showed a favourable low apparent activation energy (E_a = 4.14 kJ mol^{-1}) compared to traditional thermal approaches, which require elevated temperatures of 600–1200 °C, (E_a = 58.71 kJ mol^{-1} (Fig. S3a)).[16,17] Activation energy differences can be attributed to a high localized temperature generated on the Ni particles under irradiation, which is both highly concentrated and transient, minimizing energy losses compared to broader environmental bulky heating methods like conventional thermal or concentrated solar thermal. The intense and targeted heating at the nanoscale enhances the activation of methane molecules, resulting in a fast production rate and perfect selectivity for H_2 and multi-walled carbon nanotubes (MWCNTs). The localized heating mechanism also outperforms traditional thermal cracking by maintaining precise control over the reaction environment, reducing undesired side reactions, and optimizing catalytic efficiency with excellent selectivity for MWCNT with an outer diameter of between 10 to 50 nm (average diameter of ~17 nm) and a length of between 20 nm to 50 μm. Light-driven methane conversion benefits from reduced activation energy relative to thermal cracking. UV photons can supply discrete quanta (~430 kJ mol^{-1} for 277 nm light), directly matching the C–H bond dissociation energy, allowing selective homolytic cleavage without excessive heating.[18,19] This pathway avoids the high-temperature effects and preserves catalyst integrity. Comparatively, conventional methane thermal cracking needs more energy input to break the C–H, overheating the catalyst and causing significant chemical and/or microstructural changes, and forming amorphous carbon and mostly tip-grown CNT due to the nonuniform heat distribution during the reaction.[20,21]

Control tests were performed to monitor the activity of each component of the reaction system including the empty reactor, catalyst, and photo-grown MWCNT, to confirm catalyst optimization and rule out external contributions (Fig. 1b). 10% Ni/Al_2O_3 showed an optimum H_2 rate compared to pure Ni particles and pure MWCNT, which could be related to the metal/support interactions that improved the thermal and chemical stability of the catalyst.[22] Nickel was selected for this study as it is widely reported in the literature as the most active monometallic catalyst for methane cracking, exhibiting high methane conversion and

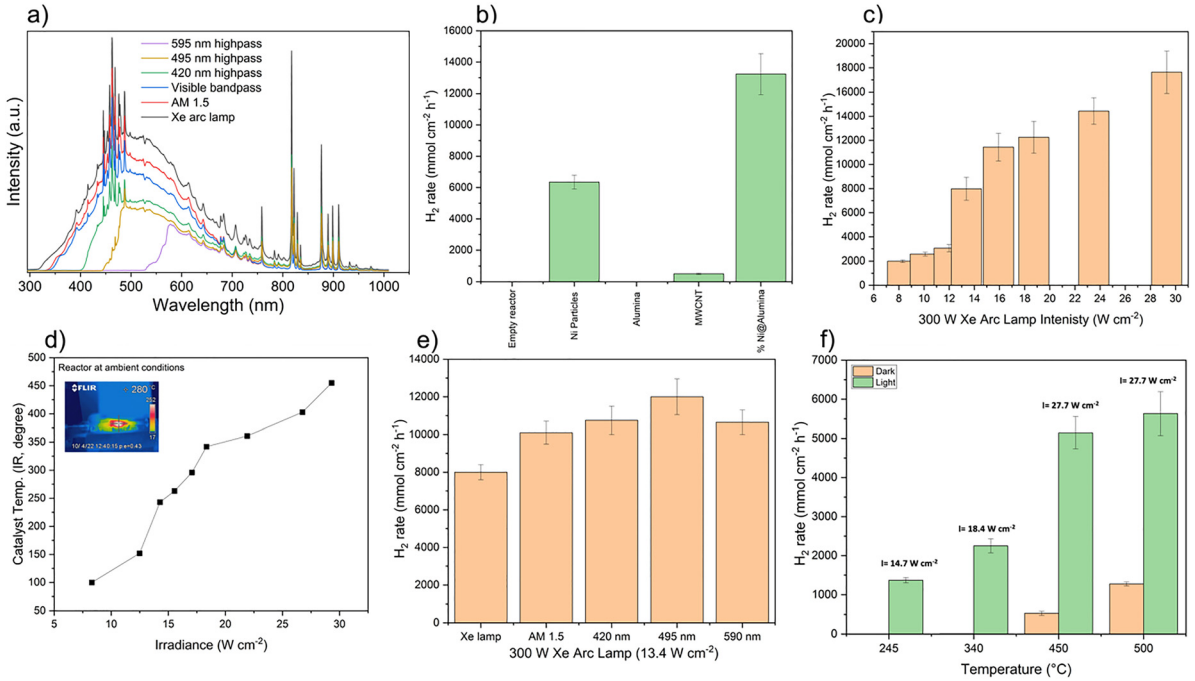

Fig. 1 Photocatalytic performance evaluation. (a) Simulated Xe light spectrum used for wavelength dependence studies. (b) Methane photolysis reaction performed on each component of the catalyst at light intensity (20 W cm^{-2}). (c) 10% Ni/Al_2O_3 sample for power intensity studies. (d) Photocatalyst surface temperature measurement under varying light intensity measured by infrared thermometry. (e) Wavelength dependence studies at irradiance (20 W cm^2). (f) The H_2 rate over 10% Ni/Al_2O_3 in the dark and heated to the corresponding temperature caused by light of different irradiance with respect to the rates under light in the same reactor configuration. In each experiment, the total gas flow was set to 20 sccm (10 sccm CH_4 : 10 sccm Ar) with an irradiated sample surface area of 0.785 cm^2. New samples were used for every test condition. At least three individual measurements were used to calculate the error bars.

hydrogen yield across a wide range of conditions.[7,23–25] Its strong activity in C–H bond activation, thermal stability, and compatibility with Al_2O_3 support made it a suitable choice for our system. That said, we have also experimentally tested Co, Fe, and Cu catalysts supported on Al_2O_3 under similar conditions (Fig. S4). Ni consistently demonstrated the highest catalytic activity and favourable formation of ordered solid carbon structures among these candidates.

Various Ni loadings on Al_2O_3 were investigated to study the effect on the H_2 rate and CNT formation (Fig. S5a). 10% Ni loading yielded MWCNT and had the highest H_2 production rate compared to 1%, 5% and 20% Ni; all catalysts have been tested under the same experimental conditions. PXRD patterns of the spent 10% and 20% Ni/Al_2O_3 showed the presence of the graphitic carbon (002) at 26.2°, while 1% and 5% did not (Fig. S5b). These results confirm the importance of the Ni particle size and distribution on photocatalytic H_2 and MWCNT formation. The influence of Ni particle size on conventional thermal methane cracking has been extensively documented in the literature.[26–30]

For this study, $Ni/\gamma\text{-}Al_2O_3$ was deliberately chosen due to its well-established strong metal–support interaction, which is widely reported to promote high dispersion of Ni particles, suppress sintering, and provide consistent methane decomposition activity and stability. Strong metal–support interaction with $\gamma\text{-}Al_2O_3$ also enables the formation of smaller Ni nanoparticles, which are more resistant to aggregation and deactivation.[31–33]

$Ni/\gamma\text{-}Al_2O_3$ additionally favors the formation of ordered carbon structures by supporting base-growth of carbon nanotubes (CNTs) for the strong metal–support interaction with better thermal stability for the gamma alumina support, facilitating separation and enhancing catalyst durability.[33] This is supported by studies showing that compared to inert (SiO_2) or basic (MgO, CaO) supports, $\gamma\text{-}Al_2O_3$ enables higher CNT quality and stability, while basic supports may favor amorphous carbon and inert supports tend to result in larger Ni particles and tip-grown CNTs with faster deactivation. Carbon-based supports can complicate mechanistic interpretation due to simultaneous carbon formation from the support itself.[34]

In addition, the acidity/basicity and high surface area of $\gamma\text{-}Al_2O_3$ facilitate the balance between catalytic activity and carbon structure, as also demonstrated in recent catalyst design studies.

We have performed direct experimental comparisons under identical conditions for 10% $Ni/\gamma\text{-}Al_2O_3$, 10% Ni/SiO_2, and 10% Ni/MgO. The results show that both $Ni/\gamma\text{-}Al_2O_3$ and Ni/SiO_2 give high hydrogen production rates, with Ni/SiO_2 the most active and Ni/MgO showing the lowest activity (Fig. S6). TEM imaging confirms that $Ni/\gamma\text{-}Al_2O_3$ supports base-grown CNTs, which allow easier CNT separation, whereas Ni/SiO_2 leads primarily to tip-growth CNTs due to weaker metal–support interactions (Fig. S7). 10% Ni/SiO_2 catalysts exhibit notably higher activity for methane photolysis than $Ni/\gamma\text{-}Al_2O_3$, under typical conditions. This increased activity is attributed to weaker metal–support interactions on SiO_2, which

expose more active nickel sites for reaction.[35] However, this same weak interaction leads to faster catalyst deactivation due to rapid carbon accumulation that blocks the nickel surfaces. In contrast, Ni/γ-Al_2O_3 demonstrates greater long-term stability and enhanced resistance to coking, owing to stronger metal–support interactions.[36] Additionally, the weak interactions in Ni/SiO_2 favor carbon nanotube (CNT) formation through tip-growth mode, which complicates product separation and diminishes CNT quality by increasing structural disorder and metal contamination[35,37] (Fig. S7b). The lowest activity of 10% Ni/Mgo is related to the strong interaction between nickel and the MgO support leads to the formation of stable NiO–MgO solid solutions or spinel-type structures, which significantly inhibit the reduction of nickel oxide to its active metallic Ni form.[38] As a result, fewer active Ni^0 sites are available to catalyze methane decomposition.[39] Additionally, the basic nature of MgO support can stabilize nickel in its oxidized state and prevent the dispersion and accessibility of metallic Ni particles, further lowering activity. Enhancing Ni/MgO activity often requires the addition of promoters such as chromium or copper, which improve the reduction of Ni and increase the number of accessible active sites.[40] In the absence of such promoters, Ni/MgO remains much less active than Ni/SiO_2 or Ni/Al_2O_3 for methane photolysis.[38–40]

The dependence of reaction rate on light intensity is a key indicator of the dominant reaction mechanism. A linear relationship typically suggests a photochemical process, where photon absorption directly generates reactive species (*e.g.*, excited electrons, radicals) that drive the reaction. In such cases, the generation rate of these species and therefore the overall reaction rate is directly proportional to the photon flux (*i.e.*, light intensity, I), and can be expressed as:

The dependence of reaction rate on light intensity

$$\text{Rate} \propto I \tag{3}$$

Each absorbed photon can initiate an elementary reaction, so doubling the light intensity approximately doubles the reaction rate, resulting in a straightforward linear correlation.[41,42]

In contrast, an exponential or super-linear dependence indicates a photothermal mechanism, where light energy is converted into localized heat, which accelerates the reaction through thermal activation. This behavior follows the Arrhenius law:

$$\text{Rate} \propto e^{\frac{-E_a}{RT}} \tag{4}$$

where E_a is the activation energy and T is the local temperature. Notably, the temperature itself increases nonlinearly (often exponentially) with light intensity due to photothermal heating effects.

In practice, both mechanisms can co-exist. The dominant pathway depends on the light intensity and the material's response to irradiation. Even a modest increase in light intensity can lead to a substantial local temperature rise, shifting the reaction behavior from photochemical to photothermal in nature.[43,44]

Varied irradiation intensities were utilized to determine the relationship between incident light intensity and H_2 production rate as well as to evaluate the relative photochemical and photothermal contributions of the 10% Ni/Al_2O_3 for methane photolysis (Fig. 1c). Incident light intensity showed a linear rate dependence and photochemical behaviour at the light intensities below 8 W cm^{-2} and an exponential Arrhenius-type photothermal behaviour at intensities above 8 W cm^{-2} (Fig. S3c and d).[45,46]

Charge separation plays a critical role in photochemical mechanisms. While our current study focuses primarily on the photothermal pathway, dominant at light intensities above 8 W cm^{-2}, further investigation into charge carrier dynamics, such as through transient absorption spectroscopy or electron paramagnetic resonance (EPR) studies, is necessary to fully disentangle and quantify photochemical contributions under lower-intensity illumination. Electron and hole scavenger experiments can provide another quantitative insight into the relative contributions of photochemical and photothermal effects in light-driven methane decomposition. As discussed in the literature,[47,48] a pronounced drop in conversion upon the addition of scavengers is indicative of photochemical involvement, whereas negligible changes confirm a dominantly photothermal mechanism.[43]

An IR camera was used to measure the bulk surface temperature of the catalyst under various light intensities in reactor with a CaF_2 window (Fig. 1d). The maximum measured temperature was 410 °C due to the intrinsic light absorbance of the material and light intensities used. Bandpass filters were used to evaluate the wavelength dependency of the reaction. Incident intensities were maintained to ensure all samples had the same incident photon flux regardless of wavelength. The total incident optical power on the sample was carefully normalized across all filter conditions, not the transmitted photon flux above the cut-off. This normalization ensures that each experiment is conducted under identical total irradiance conditions, which is a standard approach in photochemical and photothermal comparisons. 495 nm high-pass filter displayed the highest H_2 production rate and demonstrated a linear relationship between irradiation intensity and H_2 production (Fig. 1e and Fig. S3e). Our catalyst (10% Ni/Al_2O_3) has a strong and broad absorption band in the visible range (Fig. S8a), particularly between 420–600 nm, which we attribute to plasmonic coupling in Ni nanoparticles (20–80 nm).[49,50] The broadband Xe lamp (Fig. 1a) emits significant intensity in the UV, but the catalyst has relatively low absorption in this region due to a minimum near 344 nm. Shifting the light spectrum toward the visible range, either with an AM1.5 filter or long-pass filters, enhances overlap with the catalyst's strong absorption band, increasing photon absorption and thus promoting photothermal activation. Filtering out UV and blue photons ($<$495 nm) eliminates photons that are poorly absorbed or contribute primarily *via* slower, and less efficient non-radiative pathways. The remaining photons ($\geq$495 nm) coincide with the broad plasmonic absorption peak, leading to enhanced local heating *via* fast plasmonic decay processes. Furthermore, based on our Tauc analysis (Fig. S8b), the apparent optical band gap of the catalyst is $\sim$2.9 eV ($\sim$429 nm). Photons with energies above this threshold may excite interband transitions or be lost to

inefficient relaxation. In contrast, longer-wavelength photons ($\geq$495 nm) are better matched to plasmonic and free-carrier heating processes, yielding higher local temperatures and thus higher reaction rates.[51–53] As the cutoff wavelength increases beyond 590 nm, the photon energy drops below 2.1 eV, and while still within the absorption band, these photons have significantly less energy per photon. As a result, their contribution to local heating diminishes, reducing the thermal activation of methane cracking. Additionally, the optical absorption of the catalyst begins to decline past $\sim$600 nm, further limiting the efficacy of these photons in sustaining elevated reaction temperatures.

The pristine 10% Ni/Al_2O_3 samples were heated to the maximum surface temperatures measured under light irradiation by IR camera to observe the highest catalyst activity under purely thermal conditions. The reaction rates were higher under light irradiation compared to dark (Fig. 1f), confirming that photocatalysis was the driving force behind the observed activity increase.[46]

Stability under photocatalytic conditions was determined by varying incident light intensity (Fig. S9a–c). Hydrogen production rates decreased over time until it matched the activity of purely the formed carbon nanotubes. The observed decline in activity is due to the progressive blocking of active sites by the accumulated MWCNTs on the catalyst surface. This encapsulation effect reduces catalyst accessibility until the carbon deposits are removed. To evaluate the reusability of the catalyst, extensive cycling tests were performed over ten consecutive reaction cycles, as shown in Fig. S9d. After each cycle, the deposited CNT layer was mechanically removed to expose the active catalyst surface. The results clearly indicate that the hydrogen production rate gradually decreases during each run due to surface coverage by carbon deposits. However, following mechanical carbon removal, the catalytic activity was consistently restored to its initial level. These observations confirm that catalyst deactivation is primarily physical rather than chemical in nature, arising from surface blockage rather than irreversible structural or compositional degradation. Thus, the Ni/Al_2O_3 catalyst remains stable and can be readily regenerated through simple removal of the carbon layer.

To validate the scalability of our approach, we developed a customized reactor scaled 36 times larger than the bench-scale model. This advanced system incorporates a 400W white LED light source, integrated with a gas chromatograph (GC) and H_2 and CH_4 sensors, as illustrated in Fig. S10. Remarkably, the scaled-up system maintained the same selectivity for H_2 and MWCNTs (Fig. S11). These findings confirm the feasibility and practicality of our approach for large-scale hydrogen and CNT production, preserving both high selectivity and operational efficiency. We have also conducted an energy requirements calculation of our system (Fig. S12, S13 and Table S2). Our results demonstrate that our photocatalytic approach significantly reduces energy requirements, requiring approximately 70% less energy for H_2 production compared to water electrolysis and at least 74% less energy for CNT production compared to commercial methods. Additionally, our approach offers cost-effectiveness and substantial reductions in greenhouse gas (GHG) emissions, as validated through our techno-economic analysis (TEA) and life cycle assessment (LCA) (discussed in detail in a later section). These findings underscore the potential of our technology as a scalable and sustainable alternative for hydrogen and CNT production.

Optothermal modelling

The surface and bottom temperatures of the 3 mm thick catalyst pellet bed were determined experimentally and through numerical modelling (Fig. 2a and b). Both the gradient between and the absolute temperature for the surface temperature, T_1, and the bottom temperature, T_2, matched within 15 °C. Such a gradient exists as the penetration depth of the incident light from the Xe lamp is 10–100 μm, which is a much smaller depth than the 3 mm thickness of the catalyst.[54] Accurately determining the temperature-dependence of emissivity is challenging, affects thermal camera measurements, and is a possible source of deviation in the expected trend in surface temperature.[55] The thermal conductivity of the support was the dominant parameter in determining the magnitude and change in the temperature profile as a function of the power-density compared to the effect of the optical properties. Heat loss by convection had $<$10% effect on the overall temperature distribution as shown in other analysis of pellet beds.[56] The small deviation between calculated and experimental *in situ* catalyst temperatures validates experimental results from IR camera surface temperature measurements and the thermocouple measurements of the bottom of the catalyst bed. Further, the modelling quantifies the extent of light-induced heating and supports the predominance of photothermal effects and some photochemical contribution which are responsible for the formation of CNT that were absent under equivalent thermal conditions.

Rate law and Kinetic experiments

Kinetic experiments were conducted assuming a nonequilibrium batch reactor system where the total conversion of CH_4 did not exceed 10%. The conditions presented in Fig. 2c and d, where the total CH_4 conversion fulfills this requirement, were not greater than 2% at up to 2 minutes of active irradiation. The kinetic rate expressions formulated in the Materials section correspond to a reaction pathway where H_2 is formed. The rate law was expressed as a function of H_2 conversion, which depends only on the H_2 concentration, the irradiated area and reaction time. As a result, the reaction order can be described by the following equation: $Ln(rA) = Ln(k) + nLn(CA)$, where reaction order differences compared to the conventional thermal process were attributed to light effects. This suggests that the mechanism of methane photolysis could proceed independently of the reactant concentration using light.

Catalyst and CNT characterization

Transmission electron microscopy (TEM) imaging of the catalyst (10% Ni/Al_2O_3) showed deposited Ni nanoparticles with

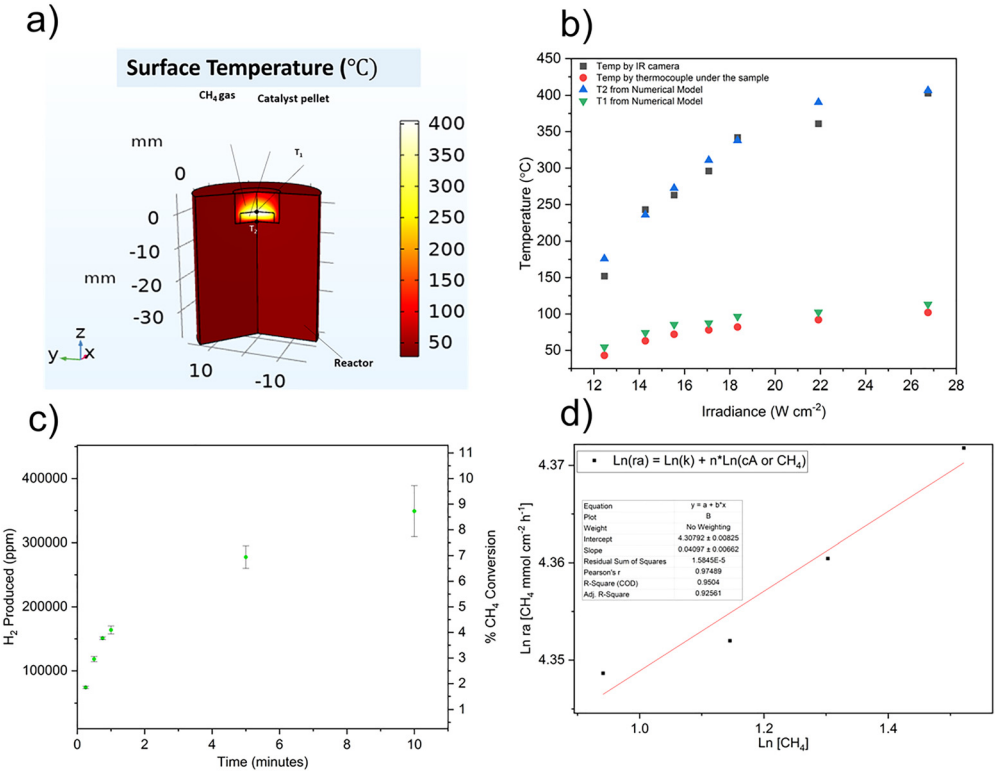

Fig. 2 Temperature measurements and kinetic experiments of the methane photolysis reaction: (a) 3-D temperature profile of 10% Ni/Al_2O_3 catalyst pellet in flow reactor cross-section (b) comparison of experimentally measured temperature of the bottom and top surface of the catalyst under different irradiances with the temperature obtained from modelling. (c) The CH_4 conversion experiment of the methane photolysis reaction over the 10% Ni/Al_2O_3. (d) The kinetic experiment of the methane photolysis reaction, where the Xe lamp light intensity was set to 10.6 W cm^{-2} in batch conditions, average pressure each test = 14.6 psi, reactor volume = 16.8 mL.

an average size of about 24 nm on the γ-alumina support (Fig. 3a and 1b). PXRD patterns confirmed catalyst crystallinity, with characteristic peaks at Ni (111), (200), and (220), in addition to the main peaks of γ-alumina. Interestingly, the PXRD pattern of the spent catalyst after light irradiation, showed the presence of well-stacked and aligned graphitic carbon (002) at 26.2 two theta (Fig. 3c).[57]

X-ray photoelectron spectroscopy (XPS) was used to determine the surface chemistry and the elemental composition of the catalyst prior to and post thermal and methane photolysis reactions. The spent catalyst post-irradiation showed more elemental carbon than the pristine sample. These results confirm the formation of the MWCNT following methane photolysis (Fig. 3d and Table S3). The sharpness of the C 1s peak in the post-methane photolysis indicates a high C–C : C=C ratio and lower C=O content compared to the pristine catalyst and confirms the ordered nature of the formed carbon (Fig. 3e). Lack of changes to the Ni 2p peaks in the high-resolution XPS spectra after methane photolysis confirms no structural change on the catalyst following reaction at low irradiation (Fig. S14).

Thermogravimetric analysis (TGA) was used to confirm the crystallinity of the formed MWCNT by measuring the sample's weight change over time as a function of temperature. Spent, fresh catalyst, and commercial MWCNT showed no thermal degradation between 150–550 °C in the amorphous carbon thermal degradation range, indicating high MWCNT crystallinity (Fig. 3f). We also conducted energy-dispersive X-ray spectroscopy (EDX) to assess the purity of the separated CNTs and quantify residual nickel and alumina impurities. Across more than 15 scanned spots, the nickel content did not exceed an average of 2%, while alumina remained below 8% (Fig. S15).

We observed that the thermal cracking of methane (methane pyrolysis) at 500 °C produced a mixture of ordered carbon, such as CNTs, and disordered carbon, like carbon black (Fig. 4a). In contrast, methane photolysis yielded only MWCNTs (Fig. 4b). The average diameter of the formed MWCNT was about 17 ± 5 nm (Fig. 2c). HRTEM images confirm the multiwalled structure of this photo-grown CNT (~40 wall) and also reveal an interlayer spacing of ~3.33 Å, similar to single crystal graphite interlayer spacing[58] (Fig. 4d and e).

I_D/I_G ratios in Raman spectroscopy identified the quality of the formed carbon.[58] High I_D/I_G indicates more disordered carbon, while low I_D/I_G ratios indicate a more ordered sp^2 hybridized carbon. The pristine catalyst showed no carbon presence and did not feature any I_D/I_G ratio (Fig. 4f). The post-irradiation spent catalyst featured a lower I_D/I_G ratio compared to post-thermal spent catalyst (Fig. 4f). Increasing the irradiance from 8 W cm^{-2} to 20 W cm^{-2} increased I_D/I_G, likely resulting from higher local temperatures under higher light intensities (Fig. 4f). The separated

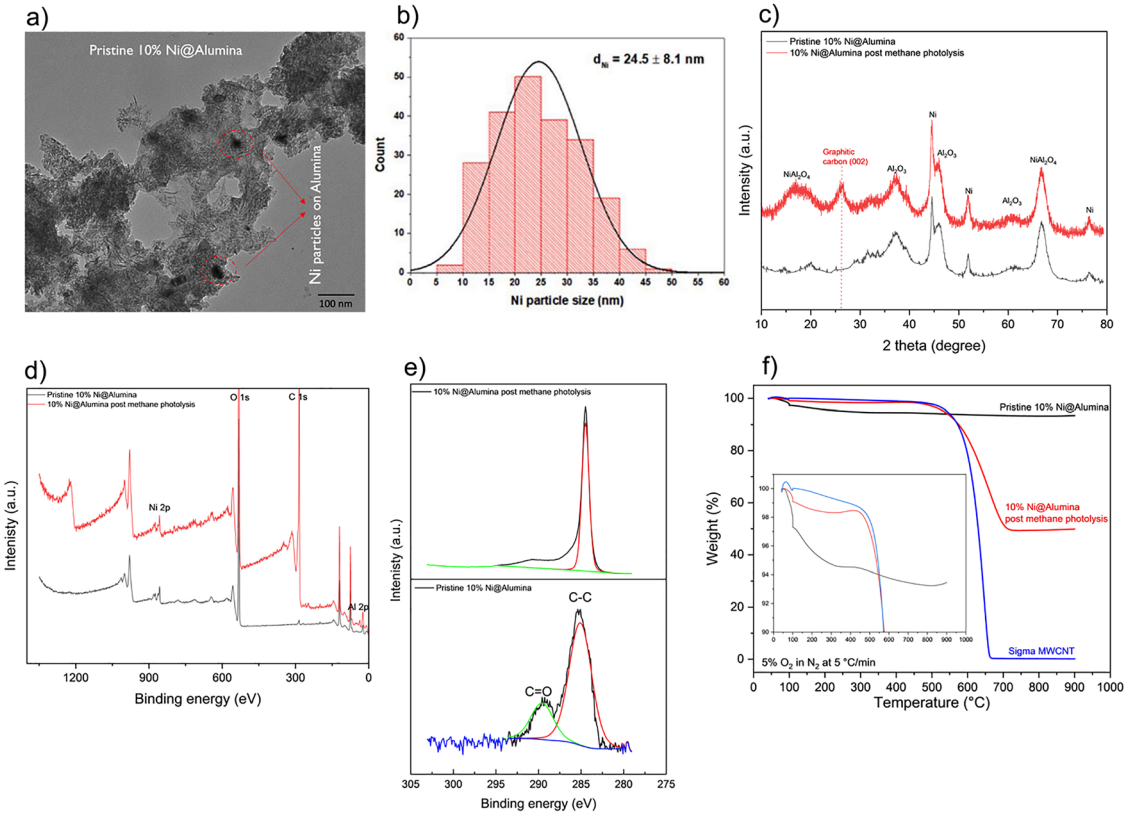

Fig. 3 Morphological and structural characterization of the 10% Ni/Al_2O_3 catalyst: (a) TEM image of the pristine catalyst; (b) particle size distribution of Ni particles, (c) XRD of the catalyst before and post the methane photolysis reaction; (d) XPS survey of the catalyst before (black line), and after the methane photolysis reaction (red line) and (e) High-resolution C1s XPS spectrum of the catalyst before and after the methane photolysis reaction and (f) TGA curves of the catalyst before and post the methane photolysis reaction compared to the commercial Sigma Corporation MWCNT sample.

MWCNT collected from the irradiated catalyst, showed a slightly higher I_D/I_G compared to commercial Sigma MWCNT due to the presence of surface oxygen functional groups (Fig. S16d).

The C 1s high-resolution XPS spectrum of the mechanically separated MWCNT showed C–C and C–OH, C═O, O-C═O and π–π* peaks at 284.3, 284.7, 286, 290 eV respectively (Fig. S16a). The O 1s high-resolution XPS spectra of the mechanically separated MWCNT confirmed the formation of oxygen functional groups (oxygen, C–O, C–OH, and C═O at 533.2, 531.6, and 530.1 eV, respectively) on the MWCNT surfaces through changes in the integrated peak areas (Fig. S16b). FTIR spectrum of the mechanically separated O-MWCNT, confirms the formation of oxygen functional groups on the MWCNT surfaces (Fig. S16c). Oxygen functionalization of MWCNT was attributed to the high local temperatures involving chemical reactions between the CNT surface and oxygen-containing species from the catalyst (Ni's high local temperature may facilitate the oxidation of CNT using oxygen from the alumina support), trace oxygen in methane (3.7 UHP Methane, 99.7%), or surface defects.[59] The high local temperature weakens and activates specific C–C and C–H bonds on the CNT surface, particularly at defect sites, edges, or unsaturated bonds, making them more reactive.[59]

Brunauer–Emmett–Teller (BET) surface area analysis and Barrett–Joyner–Halenda (BJH) pore size and pore volume distribution determined textural properties such as surface area, the pore size and pore volume distribution of the pristine and spent catalyst, and the separated MWCNT (Fig. S16, S17 and Table S5). The nitrogen adsorption–desorption isotherm of the separated MWCNTs exhibits a low uptake profile with a Type IV-like hysteresis loop (Fig. S16e), which is characteristic of mesoporous materials and commonly observed in CNT-based structures.[60] The BJH pore size distribution (Fig. S16f) reveals a broad range of pore widths extending into the macroporous region, with apparent pores >200 nm. While such macroporosity may reflect interstitial voids between entangled CNT bundles or structural heterogeneity.[61]

As expected, the fresh catalyst exhibits higher N_2 uptake than both spent samples, consistent with textural degradation resulting from CNT formation. The N_2 adsorption isotherm curve for the photolysis-treated catalyst shows more uptake, especially at higher relative pressures, indicating higher surface area and/or less pore blockage due to the formation of CNT on the former's surface (Fig. S17e). This supports our interpretation that photolysis leads to CNT formation on the external surface rather than inside pores, thereby preserving more accessible surface area compared to the pyrolysis-treated catalyst, which may be more clogged or blocked. The fresh catalyst shows a sharp peak around ~5 nm (mesopores), with a drop in pore volume after reaction (Fig. S17f). Both spent

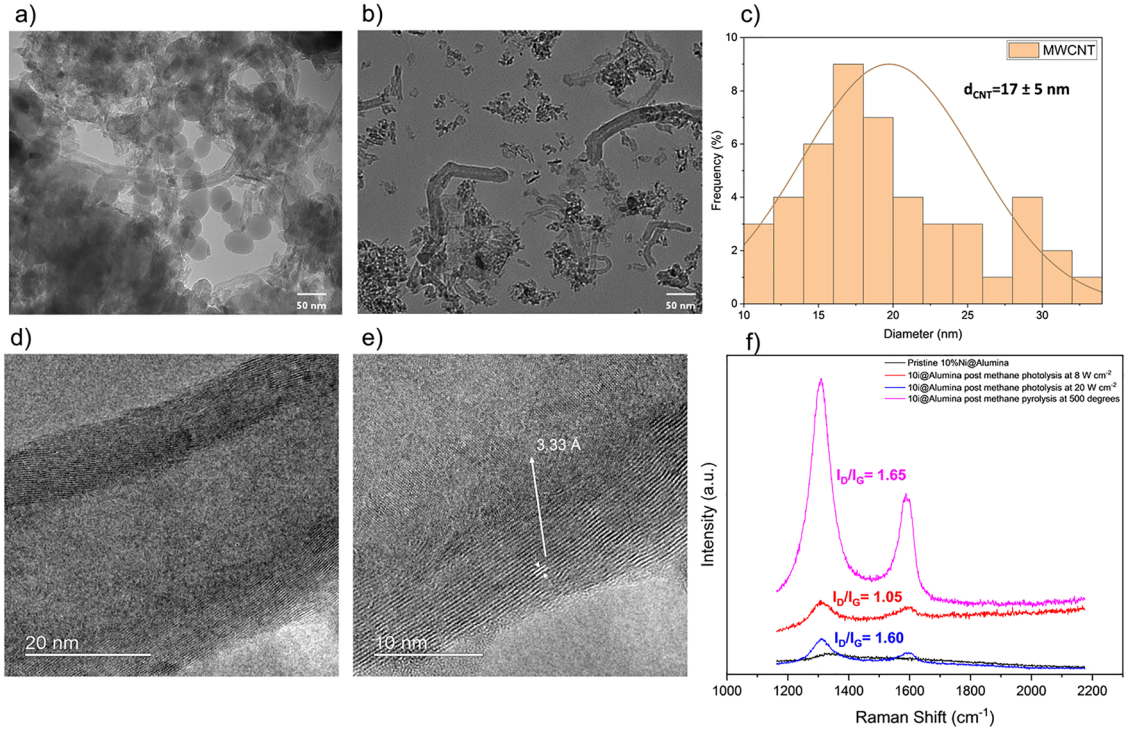

Fig. 4 Morphological and structural characterization of the photo and thermally-grown MWCNT: TEM image of (a) the catalyst post methane pyrolysis at 500 °C and (b) the catalyst post methane photolysis at a light intensity of 20 W cm^{-2}; (c) particle size distribution of MWCNT formed after methane photolysis, (d) and (e) high-resolution transmission electron microscopy (HRTEM) image of the mechanically separated MWCNT from the catalyst post methane photolysis at a light intensity of 20 W cm^{-2}, (f) Raman spectrum of the catalyst before and after the methane photolysis reaction at different light intensity and the after methane pyrolysis.

catalysts show narrowed and flattened distributions, consistent with pore blockage due to CNT deposition (Fig. S17f).

MWCNT formation mechanism

Conventional thermal methane cracking (methane pyrolysis) tends to form CNTs alongside amorphous carbon. The high temperatures required cause the Ni to detach from the support and eventually results in sintering and formation of graphitic layers rather than CNT[62] (Fig. 4a and Fig. S17a). Furthermore, nickel is difficult to separate from these tip-grown CNTs as doing so deteriorates the quality of the obtained CNT.

Comparatively, methane photolysis forms base-grown CNTs, where the metal is attached firmly to the support and the CNT stems from it (Fig. 4b and Fig. S17b). This growth difference can be attributed to high local temperatures as opposed to bulk temperatures during reactions.[63,64] High local temperatures from photothermal heating drive methane decomposition and facilitate the nucleation and growth of MWCNTs by enabling carbon atoms to diffuse and arrange themselves into cylindrical graphitic layers with enhanced crystallinity and fewer defects, thereby improving their mechanical and electrical properties and resulting in facile mechanical separation without degradation. The methane photolysis reaction over 10% Ni/Al_2O_3 can be described in three key steps: methane activation, carbon nucleation, and carbon deposition to form carbon nanomaterials.[65] Methane molecules adsorb dissociatively on the Ni metal particle surface through C–H bond photoactivation. After taking further steps, carbon atoms lead to the simultaneous release of molecular hydrogen. The adsorbed carbon atoms diffuse on the surface or through the bulk Ni metal to a suitable area for CNT formation. Previous studies in the literature showed the effect of the Ni particle size and support interaction on the formation of different carbon nanomaterials including carbon nanotubes, nano-onions, and nanofibers.[22] The base-growth mechanism can be attributed to strong Ni-support interaction forcing carbon precipitation on only the exposed surfaces of the Ni particles rather than the interface between Ni and support. This results in carbon deposition and growth on the surface of Ni particles at the gas–solid interface. As a result, the Ni particle remains fixed to the support, and close-ended MWCNT grows on the Ni surface.[22]

We have also investigated the effect of different light intensities on the formation of MWCNT. Our findings indicate that the *d*-spacing (interlayer distance) of the MWCNTs decreases from 0.38 nm to 0.33 nm as the light intensity increases from 8 to 20 W cm^{-2}, with no complete CNT formation observed at light intensities $\leq$3 W cm^{-2} (Fig. S18a). The local temperature generated by light during methane photolysis significantly influences the formation of MWCNTs and its *d*-spacing.[66–68] At low light intensities ($\leq$8 W cm^{-2}), incomplete decomposition of methane resulted in carbon atoms being deposited in a less organized fashion, leading to increased *d*-spacing of 0.38 nm due to the presence of structural defects, amorphous carbon, and weakly bound graphene layers (Fig. S18b).

As light intensity increases to 20 W cm^{-2}, high local temperatures increase methane decomposition efficiency, resulting in a higher flux of reactive carbon species. This enhances graphitization and a reduction in *d*-spacing to 0.33 nm as graphene layers form more tightly packed and well-ordered structures (Fig. S18c and d). However, excessively high light intensities can produce high local temperatures, which may cause thermal stress or non-uniform carbon deposition, potentially introducing new defects that increase *d*-spacing. Therefore, an optimal light intensity range exists for methane photolysis that minimizes *d*-spacing and maximizes the structural integrity of the MWCNTs. The increased degree of graphitization was confirmed through PXRD analysis of the spent catalyst under varying light intensities. The (002) peak intensity of the formed MWCNTs progressively increased with light intensity, indicating enhanced structural order and graphitization[69] (Fig. S3e). The Raman spectra of the MWCNTs formed at different light intensities showed an increasing I_D/I_G ratio. This change is observed when increasing the irradiance from 8 W cm^{-2} to 20 W cm^{-2} (Fig. 4f).

Computational modelling of CNT nucleation

To provide further insight for the CNT nucleation process, we used density functional theory (DFT) and its time-dependent counterpart (TD-DFT) to model a potential light-enabled reaction pathway for CH_4 conversion towards an adsorbed C_2H_2 fragment on a Ni(111) cluster-decorated γ-Al_2O_3(100) slab (Fig. S19). Since C_2 fragments are crucial in the nucleation of CNTs[70] and the edge of growing CNTs can often terminate with repeating C_2H_2 fragments,[71,72] adsorbed C_2H_2 fragments can be considered a "building block" of CNT nucleation and growth, and modelling a reaction pathway for its formation from CH_4 would provide insights into how nucleation can occur in this system. Fig. 5 shows a potential reaction pathway, with the overall reaction in the diagram given by

$$* + 2CH_4(g) \rightarrow *\_C_2H_2 + 3H_2(g)$$

where * indicates the Ni/Al_2O_3 catalyst surface and *_C_2H_2 indicates the adsorbed C_2H_2 fragment on the surface. CH_4 undergoes dissociative adsorption into adsorbed CH_3 and H, and upon the loss of H_2, the methyl fragments can couple into C_2H_6. The adsorbed C_2H_6 can then oxidatively add again to the surface Ni and proceed *via* two successive dehydrogenations to yield the adsorbed C_2H_2 fragment. The overall process is thermodynamically uphill by 2.17 eV, with energetically demanding steps for C–C bond formation (0.87 eV) and the 2nd dehydrogenation (1.36 eV).

Following the formation of adsorbed C_2H_2, subsequent additions and dehydrogenations of CH_4 can lead to an initial layer of CNT as shown in Fig. S20. In our model, proceeding from an adsorbed C_2H_2 fragment to this first layer of CNT (given by 12 sp^2 carbon atoms with C–C pairs alternating closer to and further from the surface and the pairs further from the surface capped by H atoms) corresponds to adding and releasing another 10 CH_4 and 18 H_2 molecules, respectively. The net energy change is +22.43 eV or approximately +2.24 eV for each additional carbon added.

For the two energetically demanding steps mentioned above, we further performed linear response time-dependent DFT (TD-DFT) to investigate possible pathways for light to facilitate the reaction. While the 2nd dehydrogenation is the most energetically demanding step, we found major excitations across from the computed absorption profile of the *_(C_2H_4 + 2H) intermediate (structure 9 in Fig. 5c) correspond to transitions that involve an increase in electron density on one adsorbed hydrogen and a decrease in the other, suggesting that light can help facilitate the formation of a proton and hydride towards the formation of H_2 heterolytically. We also observe transitions that involve an increase in electron density between the adsorbed C_2H_4 fragment and the Ni cluster. This suggests the light can also help facilitate a stronger bonding interaction between the carbon fragment and the metal cluster, which helps prevent the desorption of the adsorbed C_2H_4 as ethylene prematurely and allows the carbon fragment to remain on the surface for further dehydrogenation and building of the initial CNT layer. For the complete absorption profile and the selected difference densities, we refer to Fig. S21. For the *_$2CH_3$ intermediate (structure 6 in Fig. 5c), we observe multiple transitions – again within major excitations across the computed absorption spectrum (Fig. S22) – that lead to a decrease in electron density on one CH_3 fragment and an increase in another, suggesting that these excitations could help form CH_3^+ and CH_3^- fragments that facilitate heterolytic C–C coupling. Together, these results demonstrate that light plays a critical role in facilitating the key steps of CNT nucleation: C–C bond formation, dehydrogenation, and preventing early desorption of ethylene fragments.

Photo-grown MWCNT as anode for Li-ion batteries

Photo-grown and separated MWCNTs were incorporated into electrodes (Fig. 6a), assembled into half-cells with electrolyte and a separator, and then pressed into coin cells for electrochemical evaluation to demonstrate the capability for energy storage applications. To evaluate the long-term stability of the CNT electrodes, extended cycling tests were performed at 1C for 100 cycles (Fig. 6b). The CNT electrode exhibited a peak capacity of approximately 400 mAh g^{-1}. Notably, the specific capacity achieved is significantly improved compared to previous studies on CO_2-derived CNT electrodes,[73] especially considering the high C-rates applied. As the cycling continued, the capacity tended to stabilize at 350 mAh g^{-1}, with minor fluctuations. Remarkably, no abrupt voltage drop was observed at the 100th cycle, indicating effective prevention of lithium dendrite penetration and internal short-circuiting. According to Licht *et al.*,[74] the intricate interaction among CNT likely facilitates a transition from the initial dilute staging of Li^+, which occurs during the formation of LiC_6, to a mechanism combining this intercalation with a pore-

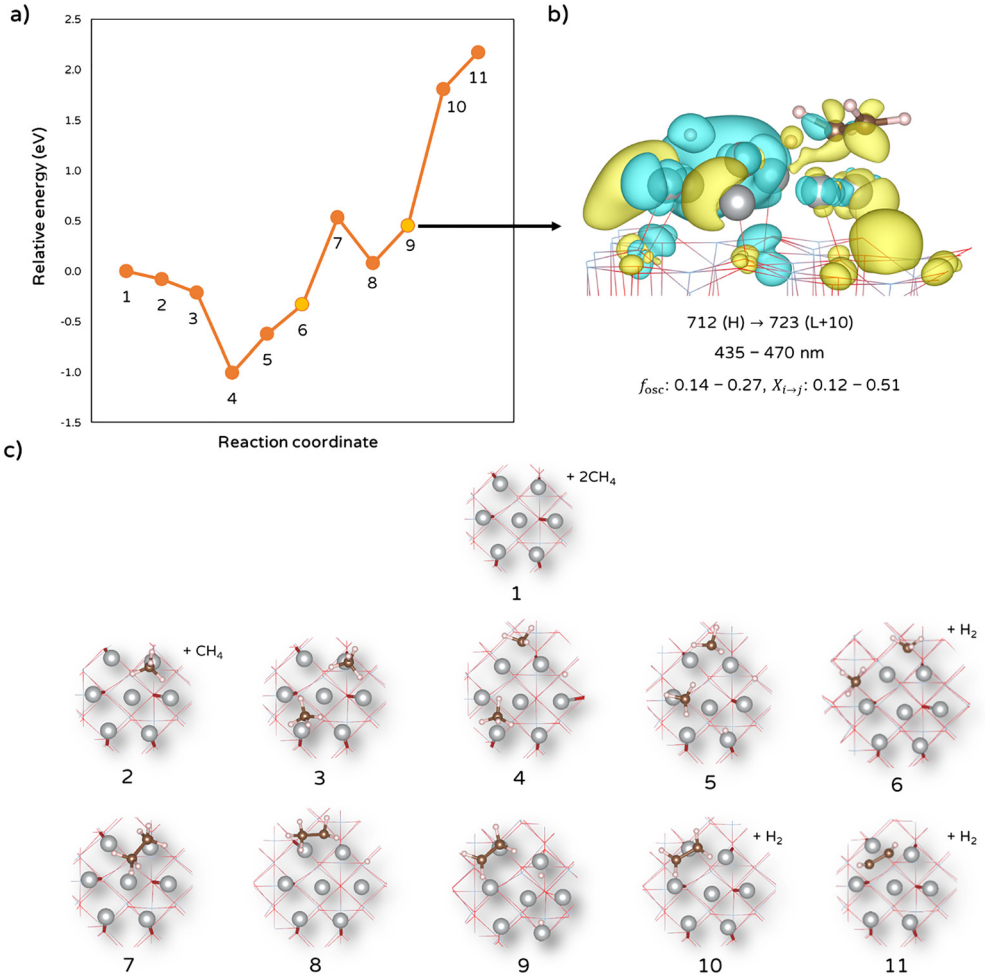

Fig. 5 DFT-computed reaction pathway for methane photolysis and CNT nucleation: (a) reaction profile for the conversion of $2CH_4$ into adsorbed C_2H_2. Numbers indicate the structures for each step found in (c), and yellow circles correspond to the intermediates where TD-DFT calculations were further carried out. (b) Representative difference density for heterolytic H_2 formation under light for the *_(C_2H_4 + 2H) intermediate (structure 9). *H*/*L* = highest/lowest occupied band/orbital, f_{osc} = oscillator strength, $X_{i\to j}$ = interband coupling constant (a number between 0 and 1 that describes how much a certain orbital pair contributes to a certain excitation), and orbital isosurface value = 0.001 e $Bohr^{-3}$ (see SI for more details). (c) Structures of each intermediate (Ni: silver, C: brown, H: white, background lines = Al_2O_3(100) surface) when viewed from atop (*i.e.* along the *c*-axis). For a full view of the model used, we refer to Fig. S11.

filling process. The progressive increase in capacity throughout cycling highlights the sustained activation of this storage.[74]

The CNT anode's initial charge capacity (during lithium insertion) closely matches its subsequent discharge capacity (during lithium extraction), suggesting a stable electrochemical performance (Fig. 6c). Notably, the self-standing anode exhibits consistent and reversible lithium-ion insertion and extraction. Furthermore, it maintains minimal voltage hysteresis over 10 cycles, demonstrating stable cycling performance and an extended cell lifetime. When compared to CNT-based anodes reported in the literature, our electrode shows lower voltage hysteresis and longer cycle life, thus demonstrating its excellent performance.[75] To investigate the reduction and oxidation behavior of the electrode, cyclic voltammetry (CV) of CNT/Li half cells was measured at 0.2 mV s^{-1}. The CV curves reveal essential processes within the cell, with significant anodic and cathodic peaks indicating Li^+ extraction and insertion, respectively.[76] The cathodic peak at ~0.03 V is attributed to the intercalation of lithium ions into graphitic layers, while the anodic peak at 0.21 V is due to the deintercalation of lithium ions (Fig. S23).[77] This observation aligns with the CV graphs reported by Liu *et al.*[78] and Zhao *et al.*,[79] which exhibited a similar trend for CNT. In the initial cycle, no new strong peaks appeared, and the peak potentials remained stable, indicating the electrochemical stability of the CNT anode across the entire voltage range.[79] The CV curves for the first three cycles mostly overlap, except for the reduction peak around ~1.0 V, which is present in the first and second cycles but disappears in the third. This suggests that the formation of the solid electrolyte interphase (SEI) effectively prevents further decomposition of the electrolyte after the initial cycles.[79]

EIS measurements were taken to evaluate the resistive properties of the electrodes, as shown in Fig. 6d. The EIS data between 2 MHz and 0.01 Hz were fitted using MEISP software based on an equivalent circuit model. The impedance information was modelled using an electrical equivalent circuit shown in the inset of Fig. 6d, which shows accurate reproductions of

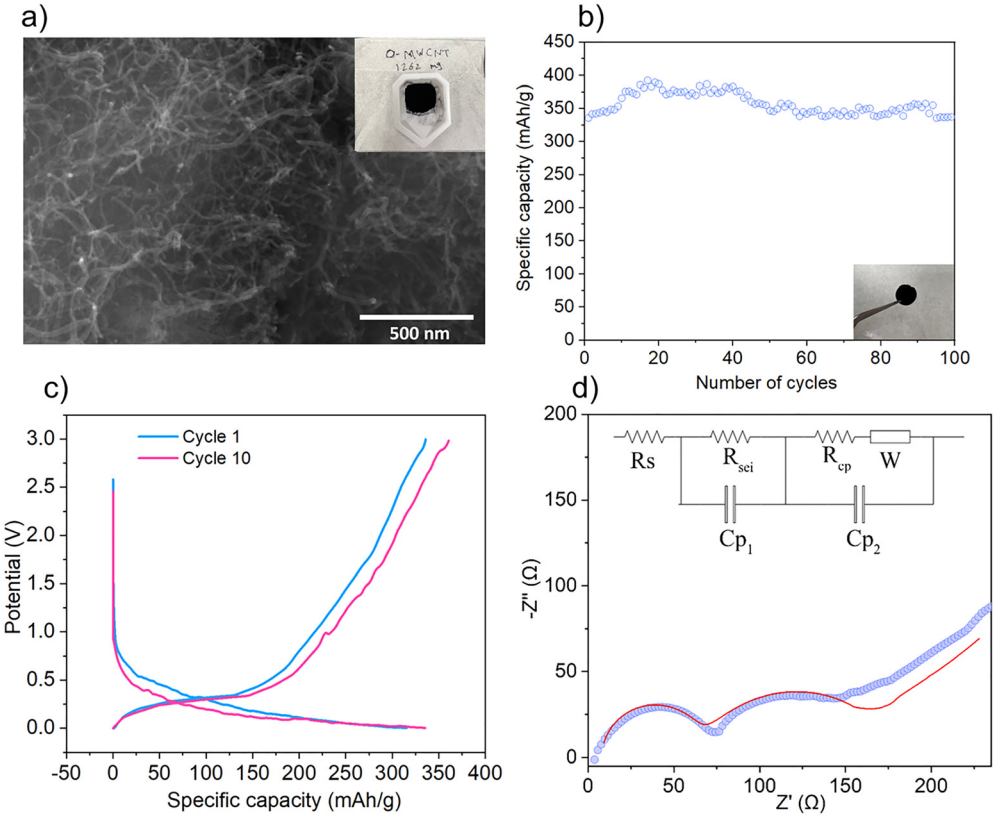

Fig. 6 (a) Morphology and electrochemical performance of MWCNT: SEM image of the mechanically separated MWCNT with an inset photo of the separated MWCNT powder. (b) Extended cycling of the MWCNT cell was performed at a current density of 1C over 100 cycles with an inset photo of the MWCNT free-standing electrode. (c) Charge/discharge profiles of MWCNT cell at 1C rate. (d) Nyquist plots of the MWCNT half-cell in the frequency range of 2 MHz to 0.01 Hz.

the arcs representing R_s, R_{ct}, and R_{sei}.[73] The intersection on the real axis at high frequency, referred to as the equivalent series resistance (R_s), indicates the combined ionic resistance of the electrolyte and the electronic resistance of the active material in the electrode. The semicircle observed at high frequencies represents the resistance of the solid electrolyte interface (R_{sei}). In addition to this high-frequency semicircle, and the mid semicircle, attributed to the charge transfer impedance between the electrolyte and the electrode, another distinct arc, identified as the low-frequency Warburg impedance tail, signifies the impedance resulting from the diffusion of ions into the active materials.[80] From the EIS fitting of the graph, it can be observed that the values of R_s, R_{sei}, and R_{ct} are 7.72 Ω, 54.76 Ω, and 119.73 Ω, respectively. The values of R_{sei} and R_{ct} demonstrate the dominance of the cell impedance, with the increase primarily attributable to charge-transfer resistance. In addition, it can be seen that R_{sei} is relatively large, indicating that the formation of the SEI plays a significant role in influencing the insertion and extraction of lithium ions.[81]

System level analysis

Process synthesis

We recently introduced a new paradigm for the design of photocatalytic processes. In contrast to using direct sunlight, a strategy that is susceptible to intermittency, variability in solar irradiance, and resulting catalyst performance, we proposed the utilization of LED-based reactors to perform photocatalytic reactions.[45] In this type of design, a 24/7 operation can be established if a constant supply of electricity can be ensured. Herein, we rely on this paradigm to develop a new process to produce hydrogen and MWCNT based on methane photolysis ($CH_4 \rightarrow 2H_2$ + MWCNT). The process consists of four main subsystems: reactor, solids separation, pressure swing adsorption, and catalyst recovery (Fig. 7(a)).

First, methane is fed to a reactor, where a supported nickel-based material is used to catalyze the photolysis reaction. The required light is supplied *via* an ancillary LED system powered by photovoltaics. The reactor system is designed considering a modular approach, in which the total number of reactor vessels (modules) is determined based on the amount of energy available per modular reactor (δ^{SE}), details on the calculation of the required number of modules are presented elsewhere.[1] To ensure a 24/7 operation, a battery system is installed. Batteries are sized based on the duration of an average night at the plant location (15.41 hours). For this study, we have chosen a place in Southern California, close to the town of Daggett. Location and night length were established based on the analysis by Peng and Maravelias.[82] The system is sized such that ~11.3 Tons H_2/h can be obtained; this size is in line with other works for the production of hydrogen and advanced carbon materials from methane.[83]

There are two reactor outlets (1) a mostly gaseous stream (stream 5) consisting of unconverted methane, hydrogen, and elutriated solids, and (2) a solid stream containing most of MWCNT and catalyst (stream 4). As MWCNT grow on the surface of the catalyst, it is necessary to remove a fraction of the catalyst from the reactor to recover this product. The small fraction of solids elutriated in the gas stream are removed using a cyclone. The gas stream without solids (stream 6), consisting of hydrogen and methane, is fed to a pressure swing adsorption (PSA) unit. This unit operates at 35 bar and produces pure hydrogen that can be sold to the market (stream 10), the PSA recovery is 85%.[83] The other outlet stream of the PSA unit consists of unconverted methane along with unrecovered hydrogen (stream 11). This stream is recycled back to the reactor. To ensure that the gas phase in the reactor consists mostly of methane, we impose a constraint limiting the fraction of hydrogen in the reactor feed to be below a predefined limit ($\delta^{H_2} = 20\%$). The solid stream produced by the reactor (stream 4) is separated into three streams, one containing catalyst (stream 13) that is recycled back to the reactor; one consisting of MWCNT (stream 12) that is collected, and a stream consisting of CO_2 (stream 14).

The process to separate the catalyst from the MWCNT is still in the early stages of development. Rather than describing a specific set of unit operations, we adopt a more general approach, in which we assume that it is possible to (1) recover a functional catalyst to be recycled once all carbon attached to its surface is removed (2) that a fraction of the carbon attached to the catalyst surface can be recovered to be sold (3) that the fraction of MWCNT that cannot be recovered from the catalyst surface can be removed *via* incineration without affecting the catalyst activity, and (4) that the catalyst has a shelf life of a year and it is replaced continuously by adding/removing new/old catalyst to/from the system. We note that the reusability of the catalyst is backed by the results presented in the experimental section. The magnitude of these streams is such that the reactor catalyst load is replaced in a year. Despite the generality of the modeling approach, we note that the system proposed is consistent with the separation scheme reported by Parmar and coworkers,[84] this scheme consists of three operations (1) sonication for the removal of the MWCNT (2) magnetic separation of the catalyst fraction (3) thermal regeneration of the catalyst to remove residual carbon.

Techno-economic analysis

We develop a non-linear model of the system to estimate mass flows and energy consumption in the different process units (see SI). The model finds the minimum selling price of the main product. Since MWCNTs are produced at a greater quantity than hydrogen (by mass) and they have a significantly larger price, we assume that they constitute the main product. Hydrogen on the other hand is produced as a valuable byproduct.

Capital costs of major pieces of equipment are estimated using different approaches: (1) for equipment commonly used in the chemical industry (cyclone, compressor) we use known cost correlations.[85] (2) For pressure swing adsorption, we use available cost estimations from the literature and the six-tenths rule for scaling.[86] (3) For batteries, we use reference costs based on DOE estimations for energy storage and a linear scaling relation[87] (4) for novel equipment requiring a tailored design (LED-based reactor and catalyst recovery system), we use a reasonable initial estimate and perform a sensitivity analysis to determine the influence that the capital cost of these pieces of equipment has on the minimum selling price of the main

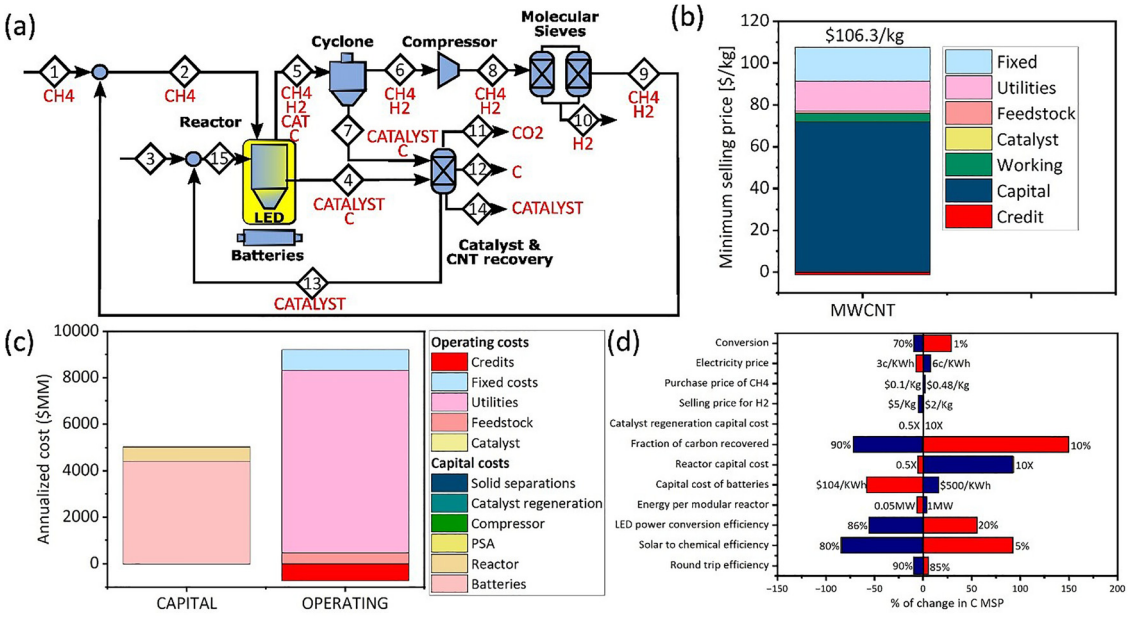

Fig. 7 (a) Layout of the process to produce hydrogen and MWCNT using methane photolysis. (b) Breakdown of the minimum selling price (c) breakdown of the capital and operating costs. (d) Sensitivity analysis to main parameters in the model, results obtained for the upper bound are shown in blue and those for the lower bound in red.

product. The operating costs of the system are estimated based on material and energy balances.

The economics of this system is a strong function of several physical/economic parameters whose value is susceptible to change as technology develops. We have grouped these parameters into five categories as shown in Table 1. The value for the parameters in the base case analysis, along with a range of possible values is shown. This range is established such we can explore the consequences of technological improvements over the next 30 years, and the effect of overoptimistic assumptions in the base case design. While the meaning of many of the parameters is evident, some of them require further explanation: The light-to-chemical efficiency (η^{CH}) denotes the fraction of energy contained in photons that is transformed into chemical energy. The LED power conversion efficiency (η^{LED}) denotes the amount of energy that is converted into light with respect to the electric energy inputs to the LED system. The energy available per modular reactor (δ^{SE}) characterizes the total amount of energy that the LED system can supply to each of the modular reactors. Finally, the fraction of carbon recovered (λ^{C}) determines the fraction of MWCNT that can be recovered as a pure and usable product. The reference values for most parameters are determined based on the current state of the art for the involved technology. For example, for roundtrip battery efficiency (η^{B}), we use a value of 85%, which is consistent with current estimations for Li-ion batteries.[87] A few of the parameters were assumed based on a reasonable estimate. Of particular importance is the fraction of carbon recovered (λ^{C}), in this case, we adopt a conservative initial estimate to reflect the uncertainty of the process. Likewise, the light-to-chemical efficiency is assumed to be 10%, a low value that can improve as better optothermal chemical reactor designs are developed.

First, we study the economics of the base case (BC). A breakdown of the minimum selling price (MSP) for the base case is shown in Fig. 7(B). An MSP of \$106.3 per kg was obtained for MWCNT assuming a hydrogen price of \$1 per kg. These results highlight the potential of the proposed technology, considering that the market price for MWCNT has been estimated to be between \$100 per kg and \$1000 per kg.[92] Furthermore, these results are obtained using the assumption of a hydrogen price of \$1 per kg, a price in line with DOE targets.[89] To further explore the relation between the MSP for the MWCNT and the hydrogen byproduct, we present a sensitivity analysis on the supplementary information (Fig. S24); we show that the MSP of MWCNT is relatively incentive to the price of H_2. For reference, if the price of H_2 drops to zero, the MSP of MWCNT increases by ~1.25%. Conversely, if the price of H_2 increases five times the MSP of MWCNT is reduced by 5.25%. The annualized capital and operating costs are shown in Fig. 7(c). The dominant operating cost is the electricity (~79%) and the dominant capital cost is the batteries (~87%). The analysis of capital cost reveals that a major limitation to the deployment of the proposed technology is the high capital investment required (~47 billion for the proposed design).

To identify the critical parameters affecting the MSF, we perform a sensitivity analysis. The results are presented in Fig. 7(c), where we show the percentage change in the MSP of MWCNT when the value of each parameter evaluated changes to the lower or upper bounds in Table 1. Since batteries dominate the capital cost and are the major component of the MSP, it is not surprising that the parameters related either to the price of energy storage (capital cost of batteries), or the amount of energy that needs to be stored (light to chemical efficiency and LED power conversion efficiency) are the most important economic drivers. In addition to these parameters, we also find that the fraction of MWCNT that can be recovered significantly influences the economics of the system. We also highlight that the capital cost of the reactor may have an important impact on the MSP if significantly larger capital costs in comparison with the base case are required. Conversely, the cost of the catalyst recovery system is not critical for the economics of the system, an increase of 10× with respect to the base case only has a marginal effect on the MSP. These results point toward the need to develop better optothermal chemical reactors for this system both requiring low capital costs and leading to a more efficient utilization of photons.

In Fig. 8, we explore the effect that incremental improvements in the parameters impacting the cost will have on the MSP. In the figure, we show both the breakdown of the MSP, and the total capital investment (TCI) required. Dramatic improvements in the MSP and TCI can be obtained if the projected improvements in key parameters are achieved. In this respect, we note that the cost of energy storage in batteries is projected to drop by more than 75% in the next 25 years.[93]

Table 1 Main parameters affecting the profitability of the process. LB: lower bound, BC: base case, UB: upper bound. All monetary values in 2021 dollars

Category	Parameter	Symbol	Units	LB	BC	UB	Ref.
LED/batteries	Round trip battery efficiency	η^{B}	%	80	85	95	87
	Light-to-chemical efficiency	η^{CH}	%	5	10	80	Assumed
	LED power conversion efficiency	η^{LED}	%	20	32.5	86	88
	Energy per modular reactor	δ^{SE}	MW	0.05	0.1	1	45
	Capital cost of batteries	θ^{B}	per KWh	104	414	500	87
	Reactor capital cost	θ^{R}	\$MM per $[kg\ s^{-1}]^{0.6}$	0.5	1	10	Assumed
Catalyst recovery	Fraction of carbon recovered	λ^{C}	%	10	25	90	Assumed
	Catalyst regeneration capital cost	θ^{CAT}	\$MM per $[kg\ s^{-1}]^{0.6}$	0.5	1	10	Assumed
Feedstock and byproduct costs	Selling price for H_2	λ^{CAT}	\$ per kg	0.5	1	10	89
	Purchase price of CH_4	λ^{CH4}	\$ per kg	0.1	0.16	0.48	90
Utilities	Electricity price	λ^{E}	\$ per KWh	0.03	0.06	0.09	91
Chemistry	Conversion	χ	%	1	8.7	90	This work

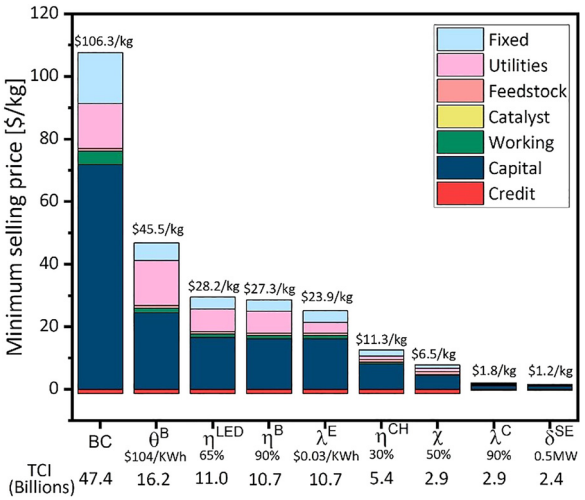

Fig. 8 Breakdown of the minimum selling price of MWCNT as a function of changes in the key parameters associated with the system.

Furthermore, the power conversion efficiency is also projected to increase to close to 86%,[88] in our calculations, we are conservative and use a more moderate 65%. Along the same lines, the efficiency of batteries has been reported to be as high as 95%,[87] but for the projection, we use a conservative 90%. Finally, we note that the SunShot target for utility-based photovoltaics electricity is $0.03 per KWh.[91] Regarding the development of our system itself, we assume three main improvements (1) that η^{CH} can be increased by 3×, this is tied to the development of better reactors (2) that conversion can be raised without major changes in selectivity to 50%, this is contingent on the development of better catalysts (3) that the fraction of carbon recovered can be as high as 90%, this depends on the design and optimization of the catalyst recovery system and (4) that the available energy per modular reactor can be increased 5×, this is also contingent on the reactor design.

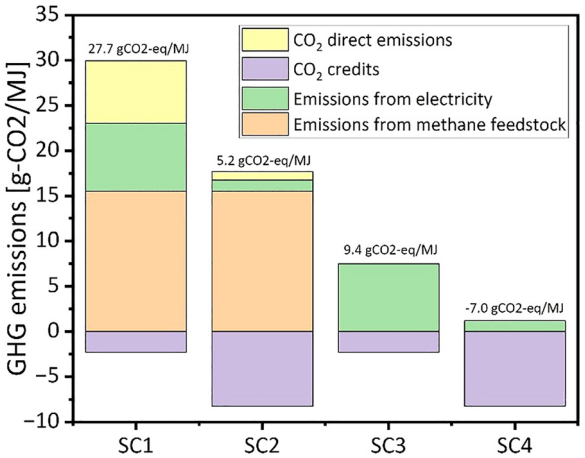

Fig. 9 Global warming potential for the proposed technology under different scenarios. S1 and S3: base case for technology, S2 and S4: best case for technology development.

There are two important conclusions from Fig. 8. First, we see that the MSP in the most optimistic case can be reduced by two orders of magnitude to as low as $1.2 per kg, this is encouraging, considering that the market price of MWCNT can drop if the offer for this type of material starts to increase as this and other competing technologies develop. The second point is that the total capital investment (TCI) will also reduce as the technologies evolve, in the most optimistic case a ∼20× reduction is observed, bringing the TCI close to 2 billion.

Life-cycle analysis

We perform a preliminary life-cycle analysis of the system to determine the global warming potential of the hydrogen produced. The functional unit used is 1 MJ of hydrogen. We assume that the carbon contained in the MWCNT can be treated as carbon credit. The PV electricity emissions factor is assumed to be ∼50 gCO_2-eq. per KWh.[94] In our analysis, four scenarios are considered (S1 to S4) (Fig. 9 and Table S5): S1 and S2 assume that the methane used comes from a fossil source. In these scenarios there is a direct non-biogenic CO_2 emission from the process, caused by the need to remove deposited carbon from the catalyst surface. S1 represents the base case technological conditions, and S2 represents the best attainable conditions according to the analysis in Fig. 8. S3 and S4 assume that the source of methane is renewable. Similarly, S3 corresponds to the base case, and S4 to the best case in terms of technological development. Cradle-to-gate factors for methane are assumed to be 8 gCO_2-eq. per KWh for fossil methane,[95] and 0 gCO_2-eq. per KWh for biomethane.[96] The results shown in Fig. 9 show that in all scenarios significant reductions in comparison with hydrogen obtained from steam methane reforming (H_2-SMR) of natural gas are obtained. For reference, emissions associated with H_2-SMR are approximately 91 gCO_2-eq. per KWh.[97] The proposed technology yields in the base case 27.7 gCO_2-eq. per KWh for fossil derived methane and 5.2 gCO_2-eq. per KWh for a renewable source. In the best-case scenario, these numbers reduce to 9.4 gCO_2-eq. per KWh and -7 gCO_2-eq. per KWh, thereby demonstrating the potential of producing carbon negative hydrogen *via* methane photocatalysis. While these results are preliminary and there is significant uncertainty associated with these early-stage calculations, we highlight that they point toward the relevance of the technology and the need for further development.

Conclusion

Currently practised thermo-chemical and plasma-chemical industrial strategies for pyrolyzing methane into hydrogen and value-added carbon nanotubes are energy and carbon intensive processes operating at temperatures greater than 900 °C. We have circumvented these extremes in light-driven process that generates clean hydrogen and high-value multi-walled carbon nanotubes. Optothermal modelling of the photocatalyst confirmed light-induced heating and the roles of photothermal and photochemical contributions to the reaction

kinetics and formation of unique reaction products absent under iso-thermal dark bulk heating conditions. The system energy requirements, carbon footprint, economics of the process, and comparison with alternatives, were evaluated by a system-level TEA–LCA in the case of intermittent solar compared to continuous LED irradiation for the co-production of clean H_2 and value-added MWCNT. We demonstrate that the light-driven pathway to these products is benefitted by a lower activation energy, lack of requirement for an external source of heat, and a zero- or even negative carbon footprint compared to alternatives. It is envisioned that the produced H_2 will fuel the emerging hydrogen economy and co-produced MWCNTs will be a commercially valuable material for battery applications as an anode in next-generation LIBs and even as an alternative for copper wires. From our TEA–LCA sensitivity study, it is projected that the light-driven process is technologically, economically, and environmentally superior to thermo- and plasma-chemical alternatives for the production of H_2 and MWCNTs.

Author contributions

A. G., M. S., and G. O. conceptualized and supervised the study. A. G. conducted catalyst and CNT characterizations, photocatalytic activity measurements, data analysis and contributed to the design and testing of the scaled up planar photoreactor system. J. M. R. performed the TEA and LCA analyses. O.D. carried out FTIR, electrochemical characterization, and battery testing for MWCNT electrodes. A. W. conducted DFT studies under A. A.-G.'s supervision. A. M. performed optothermal modeling, energy and mass balance calculations to determine the system energy requirements, and designed and conducted experiments for the scaled-up planar photoreactor system. C. V. conducted TGA measurements, kinetic experiments, contributed to the design, testing of the scaled up planar photoreactor system and data analysis. V. T. assisted with electrochemical characterization, battery testing, and data analysis. M. H. contributed to catalyst and MWCNT characterization and data analysis. J. Y. supported data analysis and proofread the manuscript. J. S. conducted Raman measurements under N. K.'s supervision. N. T. N. performed BET and BJH characterizations. All authors contributed to writing the manuscript.

Conflicts of interest

The methane photolysis and tunable photo-grown MWCNT technology is protected under U.S. Patent No. US 18/653,364 and International Patent Application No. PCT/CA2024/050776. A. G., C. V., A. M., and M. S. are co-founders of HyC Light Inc. The remaining authors declare no competing interests.

Data availability

The data supporting this study's findings are available from the corresponding author upon reasonable request.

Supplementry information (SI) is available. See DOI: https://doi.org/10.1039/d5ee02120k.

Acknowledgements

The Solar Fuels Group (https://www.solarfuels.utoronto.ca) is grateful for the financial support of the Natural Sciences and Engineering Research Council of Canada. A. G. want to thank especially John Ford, Ahmed Bobat and David Heath from the machine shop at the University of Toronto for the fantastic work building the reactors and holders used in this project. The authors acknowledge the Open Center for Characterization of Advanced Materials (OCCAM) facility for its support with HRTEM and XPS. Additionally, A. W. would like to thank the Digital Research Alliance of Canada and SciNet at the University of Toronto for providing the computational resources that enabled the DFT calculations in this work.

References

1 IEA, The Future of Hydrogen, https://www.iea.org/reports/the-future-of-hydrogen, Licence: CC BY 4.0, (accessed 17 January 2025).
2 S. Wei, R. Sacchi, A. Tukker, S. Suh and B. Steubing, *Energy Environ. Sci.*, 2024, **17**, 2157–2172.
3 K. T. Møller, T. R. Jensen, E. Akiba and H.-W. Li, *Prog. Nat. Sci.: Mater. Int.*, 2017, **27**, 34–40.
4 A. T. Ashcroft, A. K. Cheetham, M. L. H. Green and P. D. F. Vernon, *Nature*, 1991, **352**, 225–226.
5 Y. Yuan, J. Zhou, A. Bayles, H. Robatjazi, P. Nordlander and N. J. Halas, *Nat. Catal.*, 2024, **7**, 1339–1349.
6 D. C. Upham, V. Agarwal, A. Khechfe, Z. R. Snodgrass, M. J. Gordon, H. Metiu and E. W. McFarland, *Science*, 2017, **358**, 917–921.
7 N. Sánchez-Bastardo, R. Schlögl and H. Ruland, *Ind. Eng. Chem. Res.*, 2021, **60**, 11855–11881.
8 A. L. Moghaddam, S. Hejazi, M. Fattahi, M. G. Kibria, M. J. Thomson, R. AlEisa and M. A. Khan, *Energy Environ. Sci.*, 2025, **18**, 2747–2790.
9 G. Maag, G. Zanganeh and A. Steinfeld, *Int. J. Hydrogen Energy*, 2009, **34**, 7676–7685.
10 J. L. Pinilla, D. Torres, M. J. Lázaro, I. Suelves, R. Moliner, I. Cañadas, J. Rodríguez, A. Vidal and D. Martínez, *Int. J. Hydrogen Energy*, 2012, **37**, 9645–9655.
11 M. Abuseada, C. Wei, R. M. Spearrin and T. S. Fisher, *Energy Fuels*, 2022, **36**, 3920–3928.
12 G. Shu, J. Wang, B. Liu, J. Tian and Z. Liu, *Int. J. Hydrogen Energy*, 2024, **72**, 485–497.
13 R. H. Baughman, A. A. Zakhidov and W. A. de Heer, *Science*, 2002, **297**, 787–792.
14 M. Hoseinizadeh, N. Davari, A. Gouda, H. Hyat, M. Sain, D. C. Boffito and C. Santato, *Adv. Sustainable Syst.*, 2024, 2400302.
15 M. Pasquali and C. Mesters, *Proc. Natl. Acad. Sci. U. S. A.*, 2021, **118**, e2112089118.

16 H. B. Palmer and T. J. Hirt, *J. Phys. Chem.*, 1963, **67**, 709–711.
17 E. Sun, S. Zhai, D. Kim, M. Gigantino, V. Haribal, O. S. Dewey, S. M. Williams, G. Wan, A. Nelson, S. Marin-Quiros, J. Martis, C. Zhou, J. Oh, R. Randall, M. Kessler, D. Kong, J. Rojas, A. Tong, X. Xu, C. Huff, M. Pasquali, R. Gupta, M. Cargnello and A. Majumdar, *Cell Rep. Phys. Sci.*, 2023, **4**, 101338.
18 P. Wang, R. Shi, J. Zhao and T. Zhang, *Adv. Sci.*, 2024, **11**, 2305471.
19 J. Chen, S. Gao, T. Gan and B. Wang, *EcoEnergy*, 2025, **3**, e96.
20 A. M. Amin, E. Croiset, Z. Malaibari and W. Epling, *Int. J. Hydrogen Energy*, 2012, **37**, 10690–10701.
21 H. Ibrahimov, S. Malikli, Z. Ibrahimova, R. Babali and S. Aleskerova, *Appl. Petrochem. Res.*, 2021, **11**, 123–128.
22 L. Zhou, Y. Guo and K. Hideo, *AIChE J.*, 2014, **60**, 2907–2917.
23 A. M. Amin, E. Croiset and W. Epling, *Int. J. Hydrogen Energy*, 2011, **36**, 2904–2935.
24 J. C. Acomb, C. Wu and P. T. Williams, *Appl. Catal., B*, 2016, **180**, 497–510.
25 M. Msheik, S. Rodat and S. Abanades, *Energies*, 2021, **14**, 3107.
26 L. Alalga, A. Benamar and M. Trari, *Int. J. Hydrogen Energy*, 2021, **46**, 28501–28512.
27 J. A. H. Gaitan, X. Li, K. Tamura, K. Miyake, Y. Uchida and N. Nishiyama, *Adv. Energy Sustainability Res.*, 2024, **5**, 2400096.
28 W. Liang, H. Yan, C. Chen, D. Lin, K. Tan, X. Feng, Y. Liu, X. Chen, C. Yang and H. Shan, *Catalysts*, 2020, **10**, 890.
29 A. L. Dipu, *Int. J. Energy Res.*, 2021, **45**, 9858–9877.
30 A. M. S. Soliman, R. Tschentscher, D. Akporiaye and M. M. Al-Rawashdeh, *Fuel*, 2024, **368**, 131585.
31 Y. Liu, X. He, W. Mo, S. Qin, J. Guo, Y. Deng and B. Abudurehman, *ACS Omega*, 2021, **6**, 27668–27675.
32 L. He, Y. Ren, B. Yue, S. C. E. Tsang and H. He, *Processes*, 2021, **9**, 706.
33 Y. Xu, X.-H. Du, J. Li, P. Wang, J. Zhu, F.-J. Ge, J. Zhou, M. Song and W.-Y. Zhu, *J. Fuel Chem. Technol.*, 2019, **47**, 199–208.
34 I. R. Hamdani, A. Ahmad, H. M. Chulliyil, C. Srinivasakannan, A. A. Shoaibi and M. M. Hossain, *ACS Omega*, 2023, **8**, 28945–28967.
35 N. S. N. Hasnan, S. N. Timmiati, K. L. Lim, Z. Yaakob, N. H. N. Kamaruddin and L. P. Teh, *Mater. Renewable Sustainable Energy*, 2020, **9**, 8.
36 B. Yang, J. Deng, H. Li, T. Yan, J. Zhang and D. Zhang, *iScience*, 2021, **24**(7), 102747.
37 N. Patel, A. H. Fakeeha, S. B. Alreshaidan, M. F. Alotibi, A. I. Osman, A. A. H. Al-Muhtaseb, M. A. Mahyoub, R. Kumar, A. E. Abasaeed and A. S. Al-Fatesh, *Catal. Lett.*, 2024, **154**, 2475–2487.
38 H. Wang and R. T. K. Baker, *J. Phys. Chem. B*, 2004, **108**, 20273–20277.
39 A. Gamal, K. Eid, M. H. El-Naas, D. Kumar and A. Kumar, *Nanomaterials*, 2021, **11**, 1226.
40 A. Rastegarpanah, M. Rezaei, F. Meshkani, K. Zhang, X. Zhao, W. Pei, Y. Liu, J. Deng, H. Arandiyan and H. Dai, *Appl. Catal., B*, 2019, **248**, 515–525.
41 M. Fatkullin, D. Cheshev, A. Averkiev, A. Gorbunova, G. Murastov, J. Liu, P. Postnikov, C. Cheng, R. D. Rodriguez and E. Sheremet, *Nat. Commun.*, 2024, **15**, 9711.
42 C. Kerzig and O. S. Wenger, *Chem. Sci.*, 2019, **10**, 11023–11029.
43 J. Zhang, H. Chen, X. Duan, H. Sun and S. Wang, *Mater. Today*, 2023, **68**, 234–253.
44 X. Cui, Q. Ruan, X. Zhuo, X. Xia, J. Hu, R. Fu, Y. Li, J. Wang and H. Xu, *Chem. Rev.*, 2023, **123**, 6891–6952.
45 C. J. Viasus Pérez, J. M. Restrepo-Florez, J. Ye, N. T. Nguyen, A. A. Tountas, R. Song, C. Mao, A. Wang, A. Gouda, S. Corapi, S. Ji, H. MacLeod, J. Wu, A. Aspuru-Guzik, C. T. Maravelias and G. A. Ozin, *Energy Environ. Sci.*, 2023, **16**, 6155–6167.
46 P. G. O'Brien, A. Sandhel, T. E. Wood, F. M. Ali, L. B. Hoch, D. D. Perovic, C. A. Mims and G. A. Ozin, *Adv. Sci.*, 2014, **1**, 1400001.
47 Z. Liu, B. Xu, Y.-J. Jiang, Y. Zhou, X. Sun, Y. Wang and W. Zhu, *ACS Environ. Au*, 2023, **3**, 252–276.
48 A. Talebian-Kiakalaieh, E. M. Hashem, M. Guo, J. Ran and S.-Z. Qiao, *Adv. Energy Mater.*, 2025, **15**(40), e2501945.
49 V. Coello, M.-u A. Abdulkareem, C. E. Garcia-Ortiz, C. T. Sosa-Sánchez, R. Téllez-Limón and M. Peña-Gomar, *Micromachines*, 2023, **14**, 1713.
50 L. Wang, Z. Wang, L. Li, J. Zhang, J. Liu, J. Hu, X. Wu, Z. Weng, X. Chu, J. Li and Z. Qiao, *RSC Adv.*, 2020, **10**, 2661–2669.
51 L. Zhou, J. M. P. Martirez, J. Finzel, C. Zhang, D. F. Swearer, S. Tian, H. Robatjazi, M. Lou, L. Dong, L. Henderson, P. Christopher, E. A. Carter, P. Nordlander and N. J. Halas, *Nat. Energy*, 2020, **5**, 61–70.
52 S. Mukherjee, F. Libisch, N. Large, O. Neumann, L. V. Brown, J. Cheng, J. B. Lassiter, E. A. Carter, P. Nordlander and N. J. Halas, *Nano Lett.*, 2013, **13**, 240–247.
53 P. Christopher, H. Xin and S. Linic, *Nat. Chem.*, 2011, **3**, 467–472.
54 N. Heikkinen, J. Lehtonen, L. Keskiväli, J. Yim, S. Shetty, Y. Ge, M. Reinikainen and M. Putkonen, *Phys. Chem. Chem. Phys.*, 2022, **24**, 20506–20516.
55 L. Mascaretti, A. Schirato, T. Montini, A. Alabastri, A. Naldoni and P. Fornasiero, *Joule*, 2022, **6**, 1727–1732.
56 Y. Dubi, I. W. Un and Y. Sivan, *Chem. Sci.*, 2020, **11**, 5017–5027.
57 C.-Z. Yang, Y. Lou, J. Zhang, X. Xie and B. Xia, in *Materials and Working Mechanisms of Secondary Batteries*, ed. C.-Z. Yang, Y. Lou, J. Zhang, X. Xie and B. Xia, Springer Nature Singapore, Singapore, 2023, pp. 159–206, DOI: **10.1007/978-981-19-5955-4_8**.
58 O. V. Kharissova and B. I. Kharisov, *RSC Adv.*, 2014, **4**, 30807–30815.
59 R. Dubey, D. Dutta, A. Sarkar and P. Chattopadhyay, *Nanoscale Adv.*, 2021, **3**, 5722–5744.
60 E. Asedegbega-Nieto, M. Pérez-Cadenas, J. Carter, J. A. Anderson and A. Guerrero-Ruiz, *Nanoscale Res. Lett.*, 2011, **6**, 353.
61 E. T. Mombeshora, P. G. Ndungu, A. L. L. Jarvis and V. O. Nyamori, *Int. J. Energy Res.*, 2017, **41**, 1182–1201.
62 D. Ayillath Kutteri, I. W. Wang, A. Samanta, L. Li and J. Hu, *Catal. Sci. Technol.*, 2018, **8**, 858–869.

63 Z. Sun, Y. Gong, D. Cheng and Z. Sun, *J. Mater. Chem. A*, 2024, **12**, 4893–4902.
64 D. Hantoko, W. U. Khan, A. I. Osman, M. Nasr, A. K. Rashwan, Y. Gambo, A. Al Shoaibi, S. Chandrasekar and M. M. Hossain, *Environ. Chem. Lett.*, 2024, **22**, 1623–1663.
65 N. Rodriguez, *J. Mater. Res.*, 1993, **8**, 3233–3250.
66 S. Shukrullah, N. M. Mohamed, M. S. Shaharun, M. S. M. Saheed and M. I. Irshad, *Metall. Mater. Trans. A*, 2016, **47**, 1413–1424.
67 C. E. Kozonoe, V. M. Santos and M. Schmal, *Environ. Sci. Pollut. Res.*, 2023, **30**, 111382–111396.
68 I. Srikanth, N. Padmavathi, P. S. R. Prasad, P. Ghosal, R. K. Jain and C. H. Subrahmanyam, *Bull. Mater. Sci.*, 2016, **39**, 41–46.
69 Z. Zhang, W. Yang, L. Cheng, W. Cao, M. Sain, J. Tan, A. Wang and H. Jia, *ACS Sustainable Chem. Eng.*, 2020, **8**, 17629–17638.
70 M. Moors, H. Amara, T. Visart de Bocarmé, C. Bichara, F. Ducastelle, N. Kruse and J.-C. Charlier, *ACS Nano*, 2009, **3**, 511–516.
71 L. P. Ding, B. McLean, Z. Xu, X. Kong, D. Hedman, L. Qiu, A. J. Page and F. Ding, *J. Am. Chem. Soc.*, 2022, **144**, 5606–5613.
72 E. S. Penev, K. V. Bets, N. Gupta and B. I. Yakobson, *Nano Lett.*, 2018, **18**, 5288–5293.
73 Y.-H. Liu, H.-H. Lin, T.-Y. Tsai and C.-H. Hsu, *RSC Adv.*, 2019, **9**, 33117–33123.
74 S. Licht, A. Douglas, J. Ren, R. Carter, M. Lefler and C. L. Pint, *ACS Cent. Sci.*, 2016, **2**, 162–168.
75 J. Wang, H. Liu, H. Wu, Q. Li, Y. Zhang, S. Fan and J. Wang, *Carbon*, 2021, **177**, 181–188.
76 C. Pang, G. Xu, W. An, G. Ding, X. Liu, J. Chai, J. Ma, H. Liu and G. Cui, *Energy Technol.*, 2017, **5**, 1979–1989.
77 T. Zhu, Q. Hu, G. Yan, J. Wang, Z. Wang, H. Guo, X. Li and W. Peng, *Energy Technol.*, 2019, **7**, 1900273.
78 J.-Q. Liu, Q.-C. Zhuang, Y.-L. Shi, X. Yan, X. Zhao and X. Chen, *RSC Adv.*, 2016, **6**, 42885–42891.
79 L. Zhao, D. Jing, Y. Shi, Q. Zhuang, Y. Cui, Z. Ju and Y. Cui, *Ionics*, 2020, **26**, 4813–4824.
80 Q. Li, J. Ruan, S. Weng, X. Zhang, J. Hu, H. Li, D. Sun, X. Wang, F. Fang and F. Wang, *Angew. Chem., Int. Ed.*, 2023, **62**, e202310297.
81 H. Wei, H. Cheng, N. Yao, G. Li, Z. Du, R. Luo and Z. Zheng, *Chemosphere*, 2023, **343**, 140220.
82 X. Peng, T. W. Root and C. T. Maravelias, *AIChE J.*, 2019, **65**, e16458.
83 J. Riley, C. Atallah, R. Siriwardane and R. Stevens, *Int. J. Hydrogen Energy*, 2021, **46**, 20338–20358.
84 K. R. Parmar, K. K. Pant and S. Roy, *Energy Convers. Manage.*, 2021, **232**, 113893.
85 W. D. Seider, D. R. Lewin, J. Seader, S. Widagdo, R. Gani and K. M. Ng, *Product and process design principles: synthesis, analysis, and evaluation*, John Wiley & Sons, 2017.
86 E. Lewis, S. McNaul, M. Jamieson, M. S. Henriksen, H. S. Matthews, L. Walsh, J. Grove, T. Shultz, T. J. Skone and R. Stevens, *Comparison of commercial, state-of-the-art, fossil-based hydrogen production technologies*, National Energy Technology Laboratory (NETL), Pittsburgh, PA, Morgantown, WV. . ., 2022.
87 W. Cole, A. W. Frazier and C. Augustine, *Cost projections for utility-scale battery storage: 2021 update*, National Renewable Energy Lab.(NREL), Golden, CO (United States), 2021.
88 P. M. Pattison, M. Hansen and J. Y. Tsao, *C. R. Phys.*, 2018, **19**, 134–145.
89 S. Johnson, P. Sabharwall and Y. Ballout, *Next Energy*, 2023, **1**, 100070.
90 Henry Hub Natural Gas Spot Price (Dollars per Million Btu), **https://www.eia.gov/dnav/ng/hist/rngwhhdm.htm**, (accessed 6/5/2024).
91 SunShot 2030, Solar Energy Technologies Office, **https://www.energy.gov/eere/solar/sunshot-2030#:~:text = The%20goals%20cut%20the%20levelized,market%20barriers%20in%20order%20to**, (accessed 09/06, 2024).
92 R. A. Dagle, V. Dagle, M. D. Bearden, J. D. Holladay, T. R. Krause and S. Ahmed, An Overview of Natural Gas Conversion Technologies for Co-Production of Hydrogen and Value-Added Solid Carbon Products, Pacific Northwest National Lab. (PNNL), Richland, WA (United States), Argonne National Lab. (ANL), Argonne, IL (United States), United States, 2017.
93 T. Aquino, M. Roling, C. Baker and L. Rowland, Battery Energy Storage Technology Assessment, Platte River Power Authority, Fort Collins, CO, USA, 2017.
94 L. C. Stages, *J. Ind. Ecol.*, 2012, 56.
95 T. J. Skone, J. Littlefield, J. Marriott, G. Cooney, L. Demetrion, M. Jamieson, C. Jones, M. Mutchek, C. Y. Shih and G. Schivley, *Life cycle analysis of natural gas extraction and power generation*, National Energy Technology Laboratory (NETL), Pittsburgh, PA, Morgantown, WV. . ., 2016.
96 S. Kolb, T. Plankenbühler, K. Hofmann, J. Bergerson and J. Karl, *Renewable Sustainable Energy Rev.*, 2021, **146**, 111147.
97 G. Reiter and J. Lindorfer, *Int. J. Life Cycle Assess.*, 2015, **20**, 477–489.

